nature physics

ARTICLES

https://doi.org/10.1038/s41567-021-01238-8

Check for updates

Active phase separation by turning towards regions of higher density

Jie Zhang[1,8], Ricard Alert[2,3,8], Jing Yan[4], Ned S. Wingreen[2,5] and Steve Granick[6,7] ✉

Studies of active matter, from molecular assemblies to animal groups, have revealed two broad classes of behaviour: a tendency to align yields orientational order and collective motion, whereas particle repulsion leads to self-trapping and motility-induced phase separation. Here we report a third class of behaviour: orientational interactions that produce active phase separation. Combining theory and experiments on self-propelled Janus colloids, we show that stronger repulsion on the rear than on the front of these particles produces non-reciprocal torques that reorient particle motion towards high-density regions. Particles thus self-propel towards crowded areas, which leads to phase separation. Clusters remain fluid and exhibit fast particle turnover, in contrast to the jammed clusters that typically arise from self-trapping, and interfaces are sufficiently wide that they span entire clusters. Overall, our work identifies a torque-based mechanism for phase separation in active fluids, and our theory predicts that these orientational interactions yield coexisting phases that lack internal orientational order.

We are interested here in motile ('self-propelled') agents. As motility naturally implies direction, alignment interactions lead to collective motion, with flocking as an iconic example. When the motility direction is not coordinated, self-propelled particles are well understood to undergo motility-induced phase separation (MIPS) under certain conditions[1–6]. As originally conceived[7], the mechanism of MIPS is self-trapping: lower particle speed in high-density regions, due to quorum sensing[7,8] or even just due to repulsive particle collisions[9–11], promotes continual accumulation of particles. This positive feedback leads to phase separation into a dilute gas and denser clusters. In the past decade, this scenario has been widely studied using theory and simulations[1–6]. Proposals to realize this scenario using synthetic active colloids[4,12–14] indeed led to the observation of motility-dependent clustering[15–18]. Eliminating the possible role of attractive interactions, recent experiments with purely repulsive colloids have confirmed full phase separation[19], or separation interrupted by the effects of aligning interactions[20].

Here we show that torques on motile particles can induce phase separation. This finding is surprising because torques can easily prevent MIPS. For example, rod-shaped particles experience torques that favour alignment, thereby avoiding self-trapping and suppressing MIPS[21–25]. Other kinds of orientational interaction, including dipolar torques[20,26,27] and velocity-alignment rules[28–31], can either hinder or promote standard repulsion-based MIPS. Unlike conventional MIPS, torque-based aggregation requires no density-induced slowdown, so the particles that condense into clusters retain substantial speed. As a result, clusters remain fluid, as opposed to the close-packed and jammed clusters typically obtained in repulsion-based MIPS[9–11,19,20]. Consequently, this alternative mechanism of phase separation has the potential to enlarge resulting group functions, such as fast turnover of active agents and efficient exchange of information.

Active phase separation in metal–dielectric Janus colloids

Here we combine theory and experiments on self-propelled Janus particles driven by induced charge electrophoresis. The particles are 3-μm-diameter silica spheres, coated with titanium (Methods) on one hemisphere. These particles are suspended in a 0.05 mM NaCl aqueous solution and placed between conductive coverslips coated with indium tin oxide, separated by a 120 μm spacer (Fig. 1a and Methods). Particles sediment to form a dilute monolayer with area fraction in the range $\phi_0 \approx 0.05–0.15$. To drive the particles, we apply a perpendicular a.c. voltage of amplitude $V_0 = 8–10$ V and frequency $\nu = 30$ kHz. The resulting electric field tends to align the particle equator perpendicular to the coverslips. The resulting unequal electric polarization on the metal and dielectric hemispheres (Fig. 1b) induces electrokinetic flows that produce particle self-propulsion[32–34] (along a direction $\hat{\mathbf{n}}$ pointing from the metallic to the dielectric hemisphere), as well as electrostatic interparticle forces and torques (Fig. 1b).

Clusters, observed within seconds of switching on the electric field, coarsen in a process suggestive of Ostwald ripening, with large clusters growing and small clusters shrinking and disappearing (Supplementary Video 1 and Extended Data Fig. 1). Domain-growth kinetics are compatible with the Lifshitz–Slyozov relation $L(t) \sim t^{1/3}$ of classic phase separation, where L is the domain size and t the time (Fig. 1c), consistent with the mapping to an effective free energy that we present below.

As it was not possible experimentally to avoid some particles being stuck on the coverslip, it was natural to enquire whether clusters necessarily nucleated around them. This possibility was discounted, as at early times the majority of clusters encompassed no stuck particles (Extended Data Fig. 2). On the other hand, during coarsening a large fraction of clusters contain a few particles that are stuck on the coverslip, which might help form and stabilize the clusters (Extended Data Fig. 2).

[1]Department of Physics, University of California at Santa Barbara, Santa Barbara, CA, USA. [2]Lewis-Sigler Institute for Integrative Genomics, Princeton University, Princeton, NJ, USA. [3]Princeton Center for Theoretical Science, Princeton University, Princeton, NJ, USA. [4]Department of Molecular, Cellular and Developmental Biology, Yale University, New Haven, CT, USA. [5]Department of Molecular Biology, Princeton University, Princeton, NJ, USA. [6]Center for Soft and Living Matter, Institute for Basic Science (IBS), Ulsan, South Korea. [7]Departments of Chemistry and Physics, Ulsan National Institute of Science and Technology (UNIST), Ulsan, South Korea. [8]These authors contributed equally: Jie Zhang, Ricard Alert. ✉e-mail: sgranick@gmail.com

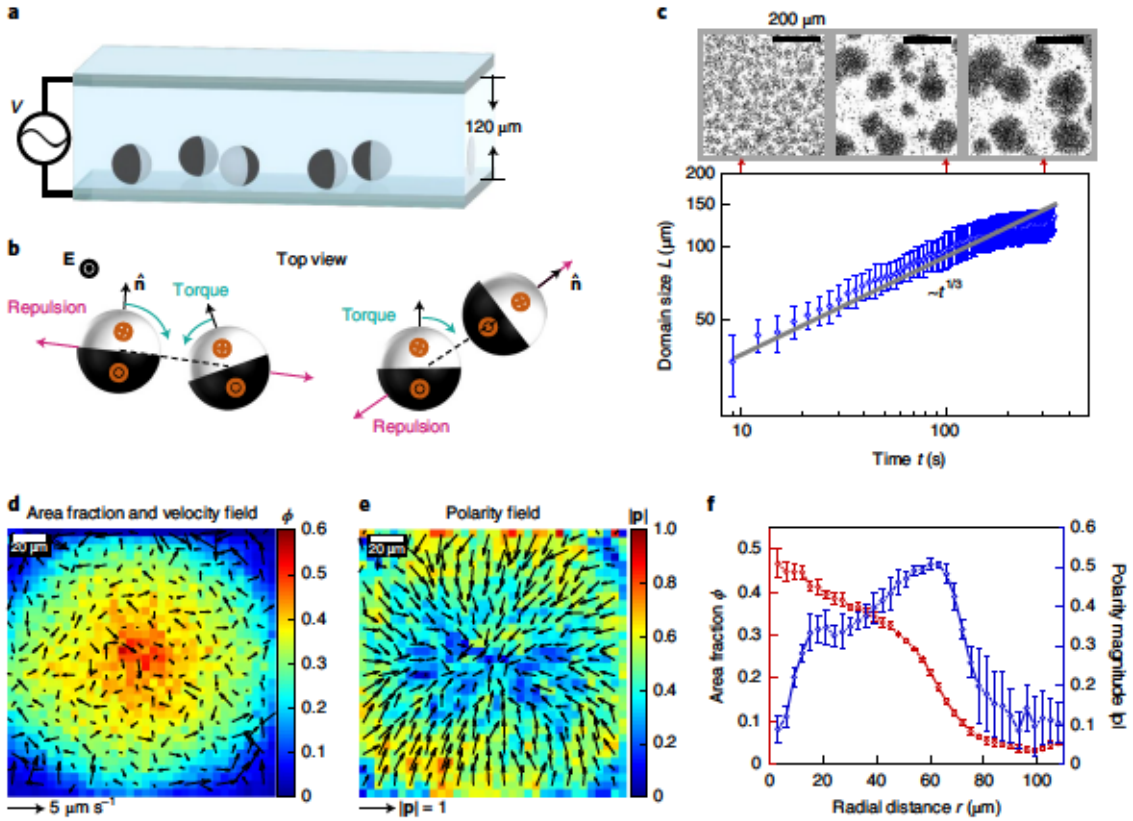

Fig. 1 | Active phase separation in metal–dielectric Janus colloids. a, Schematic of the experimental set-up in which 3-μm-diameter particles are allowed to sediment in water to the bottom of a sample cell across which a.c. electric fields are applied vertically. **b**, Top view of two Janus particle pairs in an electric field that induces dipoles of opposite orientations and different magnitudes (orange) on the head and tail hemispheres. This leads to particle self-propulsion along the direction $\hat{\mathbf{n}}$ (black), and to interparticle forces (purple) and torques (green). Torques rotate particles in the direction of the interparticle distance, which is indicated by the dashed line. These torques are generally non-reciprocal. **c**, Clusters coarsen (Supplementary Video 1, 30 kHz, 83 V mm^{-1}) with domain-growth kinetics compatible with the Lifshitz–Slyozov relation $L(t) \sim t^{1/3}$. Error bars are s.d. over four independent experiments. **d**,**e**, Time-averaged local area fraction (**d**, colour), along with velocity field (**d**, arrows) and polarity field (**e**, arrows with magnitude in colour) in a cluster (30 kHz, 66 V mm^{-1}). Averaging is over 36 μm^2 square bins over 50 s (2,500 frames), during which the number of particles in the cluster remains approximately constant (Extended Data Fig. 4). **f**, Angle-averaged radial profiles of area fraction (red) and polarity magnitude (blue) corresponding to **d** and **e**. Error bars are s.d.

Clusters have wide interfaces

Despite the familiar coarsening kinetics, the structure and dynamics of individual clusters differ markedly from those observed in passive phase separation and repulsion-based MIPS. Rather than displaying the standard uniform bulk and sharp interface, our clusters exhibit a pronounced density gradient (Fig. 1d, Extended Data Fig. 3 and Supplementary Video 2) and inward-pointing polarity (Fig. 1e), defined as $\mathbf{p} = \langle \hat{\mathbf{n}} \rangle$. Particle density increases from the edge to the centre without a density plateau (Fig. 1f, red) for clusters up to ~300 μm in diameter, suggesting very wide interfaces, at least several tens of micrometres. The central density (area fraction $\phi \approx 0.6$) never approaches close packing. Reciprocally, polarity $|\mathbf{p}|$ is highest at the cluster edge and decreases towards the centre (Fig. 1f, blue). This decrease suggests that clusters might eventually grow large enough to develop an isotropic ($\mathbf{p} = \mathbf{0}$) bulk phase. The inward-pointing polarity at clusters' edges prevents them from coalescing immediately upon contact. Rather, upon collisions between clusters, visible boundaries persist for minutes in some cases (Supplementary Video 1; see snapshots in Fig. 1c).

Non-jammed clusters with fast particle turnover

The dynamics of individual particles within clusters differs markedly from that in jamming-based MIPS: clusters are fluid, not jammed. Particles move easily through clusters (Supplementary Video 3), which exhibit fast turnover, with particles leaving and joining a cluster on a timescale of tens of seconds (Fig. 2a and Extended Data Fig. 4). The number of native particles that remain in a cluster decays exponentially with a characteristic time depending on the cluster size and particle speed (Fig. 2b, Extended Data Fig. 5 and Supplementary Video 4). By tracking the position and orientation of particles at different local ϕ, we obtain their mean square translational and angular displacements (Extended Data Fig. 6). From these measurements, we find that particles within clusters ($\phi > 0.1$) are slower than those outside them ($\phi < 0.1$), but do not slow down further at the higher densities deeper inside clusters (Fig. 2c, red). On the other hand, the effective rotational diffusivity D_r^{eff} increases monotonically with local area fraction (Fig. 2c, blue), indicating faster particle reorientations due to stronger interparticle torques in denser regions.

Flickering chains facilitate particle motion

Since head and tail particle hemispheres attract each other (Fig. 1b), particles in clusters often form chains, three to seven particles long, which last hundreds of milliseconds (Supplementary Video 5 and red lines in Fig. 3a). These chains constantly deform, break and reform, with particles hopping on and off different

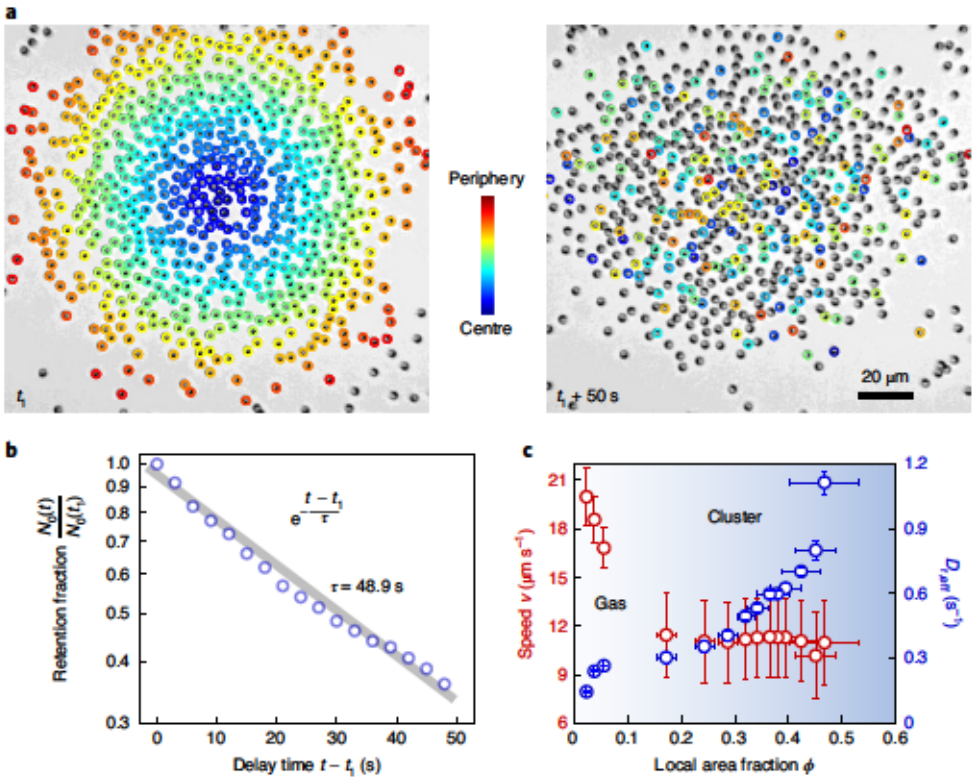

Fig. 2 | Particle turnover dynamics of non-jammed clusters whose population remains nearly constant. a, Example of particle turnover between the gas and cluster states for a cluster whose total population is nearly constant over the experimental time window (Supplementary Video 3). The first snapshot shows the cluster at an initial time $t = t_1$, chosen arbitrarily, with particles coloured according to their distance from the cluster centroid. In the second snapshot, 50 s later, particles have moved through the cluster and turned over. **b**, Particle retention dynamics. The fraction of initial particles that remains within the cluster decays exponentially with elapsed time. **c**, Average particle speed (red) and effective rotational diffusivity (blue) within the gas and cluster states, as functions of the local area fraction. The three points at low ϕ (<0.1) correspond to the gas state. Increasingly higher area fractions correspond to regions deeper into clusters. The speed and effective rotational diffusivity are obtained from the first 0.5 s of the translational and angular mean squared displacements, respectively (Extended Data Fig. 6). Averaging is over 50 s (2,500 frames) in the cluster shown in **a**. Error bars are s.d.

chains. To characterize positional and orientational order, we measure the pair distribution function $g(\mathbf{r}) = \phi(\mathbf{r})/\phi_0$ and the orientation correlation function $C(\mathbf{r}) = \langle \hat{\mathbf{n}}(\mathbf{r}') \cdot \hat{\mathbf{n}}(\mathbf{r}' + \mathbf{r}) \rangle$. As expected for self-propelled particles, $g(\mathbf{r})$ is anisotropic: it is more likely to find another particle ahead than behind a reference particle (Fig. 3b). We also find that it is more likely to find another particle behind than on the side of the reference particle, producing a depletion wing pattern (Fig. 3c). While recent work showed that these depletion wings can arise even in the absence of alignment interactions[35], in our system they result from torques generated by head–tail attraction. Finally, orientational correlations are stronger along the direction of self-propulsion than perpendicular to it (Fig. 3c), showing that particles tend to align along the chains, but not with lateral neighbours.

Particle orientation and velocity are misaligned in clusters

Despite these transient chains, particle motion is disordered at long times, as shown by the time-averaged velocity field (Fig. 1d, arrows). Interestingly, this lack of velocity order coexists with radial polar order (Fig. 1e). This distinction is apparent in the probability distributions of the angles formed by the particle orientation and velocity with respect to the clusters' radial direction (Fig. 3d): whereas the orientation angle distribution peaks at 0 (Fig. 3e, blue), consistent with radial order, the velocity angle distribution peaks at $\pm\pi/2$ (Fig. 3e, red), indicating flows orthogonal to the radial direction. That is, even though particles orient mainly towards the centre of the cluster, they have a higher chance to move tangentially to it. As expected, the difference between orientation and velocity angles is absent before cluster formation (Extended Data Fig. 7), but emerges from the stronger interparticle interactions within clusters (Fig. 3f).

Model for Janus particles with electrostatic interactions

As our experiments show MIPS without substantial self-trapping, non-standard mechanisms might be responsible for phase separation in our system. We therefore developed a microscopic model based on the dipolar interactions between the hemispheres of our particles (Supplementary Note A). Our model shows that two particles interact via a repulsive force

$$\mathbf{F}_{ij} \approx \frac{3}{4\pi\varepsilon} \frac{(d_h + d_t)^2}{r_{ij}^4} e^{-r_{ij}/\lambda} \hat{\mathbf{r}}_{ij}, \quad (1)$$

where ϵ is the dielectric permittivity of the solvent, $\mathbf{r}_{ij} = \mathbf{r}_j - \mathbf{r}_i$ is the interparticle distance vector and $d_h < 0$ and $d_t > 0$ are the effective dipole strengths of the head and tail hemispheres, respectively (Fig. 1b). The exponential factor accounts for screening by the electrodes, separated by a distance $\lambda = 120\,\mu$m. Moreover, because tail dipoles are stronger than head dipoles ($d_t^2 > d_h^2$), particles interact via a torque

$$\mathbf{\Gamma}_{ij} \approx \frac{3\ell}{4\pi\varepsilon} \frac{d_h^2 - d_t^2}{r_{ij}^4} e^{-r_{ij}/\lambda} \hat{\mathbf{n}}_j \times \hat{\mathbf{r}}_{ij}, \quad (2)$$

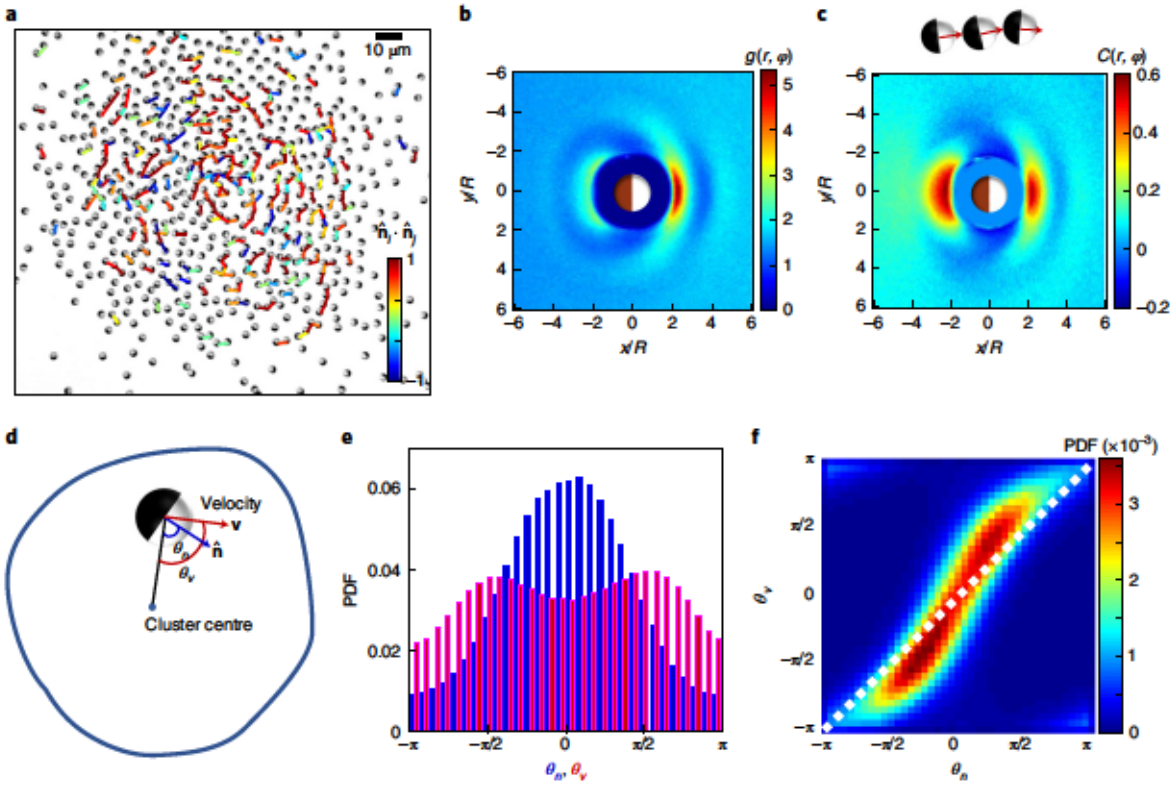

Fig. 3 | Particle orientation, velocity and correlations in non-jammed clusters. a, Snapshot of a cluster, overlaid with lines connecting pairs of particles whose centres are separated by less than three particle radii. The colour shows the degree of pair alignment, with red indicating chaining. **b**,**c**, Pair distribution function $g(\mathbf{r})$ (**b**) and orientation correlation function $C(\mathbf{r})$ (**c**) averaged over the cluster for 50 s (2,500 frames), showing the tendency of particles to line up and align in chains, respectively. Coordinates are scaled by the particle radius. **d**, Definitions of the angle formed by particle orientation (θ_n) and velocity (θ_v) with respect to the radial direction. Schematically, the blue contour indicates the cluster periphery. **e**,**f**, Individual (**e**) and joint (**f**) probability distribution functions (PDFs) of the orientation and velocity angles defined in **d**. In **f**, deviation from the diagonal shows misalignment between particle orientation and velocity.

where $\ell = 3R/8$ is the distance by which the dipoles are off centred, with $R = 1.5\,\mu$m the particle radius. This torque tends to reorient the particles in the direction of $\mathbf{r}_{ij}$ (Fig. 1b). Hence, it is responsible for chain formation (Fig. 3); particles aligned in a chain experience no torque because they point along $\mathbf{r}_{ij}$ (Fig. 1b, right). Even though the underlying forces between dipoles are reciprocal, the torques $\mathbf{\Gamma}_{ij}$ between particles are in general non-reciprocal: $\mathbf{\Gamma}_{ij} \neq -\mathbf{\Gamma}_{ji}$. Whereas one particle may be already aligned with $\mathbf{r}_{ij}$, the other one may not (Fig. 1b, right). As two particles reorient in a non-reciprocal way, they also rotate around their common centre of mass (Supplementary Note A). Experimentally, torque non-reciprocity manifests in the dynamics and statistics of two-particle interaction events (Extended Data Fig. 8).

We write Langevin equations for the translational and rotational motion of particle i as

$$\frac{\mathrm{d}\mathbf{r}_i}{\mathrm{d}t} = v_0\hat{\mathbf{n}}_i + \frac{\mathbf{F}_i}{\xi_\mathrm{t}} + \boldsymbol{\eta}_i^\mathrm{t}(t); \qquad \mathbf{F}_i = \sum_{j\neq i}\mathbf{F}_{ji} \tag{3a}$$

$$\frac{\mathrm{d}\hat{\mathbf{n}}_i}{\mathrm{d}t} = \frac{\mathbf{\Gamma}_i}{\xi_\mathrm{r}} + \boldsymbol{\eta}_i^\mathrm{r}(t); \qquad \mathbf{\Gamma}_i = \sum_{j\neq i}\mathbf{\Gamma}_{ji} \tag{3b}$$

where v_0 is the self-propulsion speed, ξ_t and ξ_r are the translational and rotational friction coefficients, respectively, and $\boldsymbol{\eta}_i^\mathrm{t}(t)$ and $\boldsymbol{\eta}_i^\mathrm{r}(t)$ are both Gaussian white noise (Supplementary Note A).

Collective forces and torques

To predict the collective behaviour of the system, we coarse-grain the microscopic model (Supplementary Note B) and obtain the Smoluchowski equation for the probability $\Psi_1(\mathbf{r}, \hat{\mathbf{n}}; t)$ of finding a particle at position $\mathbf{r}$ and orientation $\hat{\mathbf{n}}$ at time t (Supplementary equation (24)). This probability evolves under the action of collective interaction forces and torques that depend on the particle density field $\rho(\mathbf{r})$ (refs. [5,36,37]). To first order in density gradients, we obtain (Supplementary Note B)

$$\mathbf{F}_\mathrm{int}(\mathbf{r}, \hat{\mathbf{n}}) = -\Psi_1(\mathbf{r}, \hat{\mathbf{n}})\left[\zeta_0\rho(\mathbf{r})\hat{\mathbf{n}} + \zeta_1\nabla\rho(\mathbf{r})\right], \tag{4a}$$

$$\mathbf{\Gamma}_\mathrm{int}(\mathbf{r}, \hat{\mathbf{n}}) = \Psi_1(\mathbf{r}, \hat{\mathbf{n}})\,\tau_1\,\hat{\mathbf{n}}\times\nabla\rho(\mathbf{r}). \tag{4b}$$

The coefficients $\zeta_0, \zeta_1, \tau_1 > 0$ (Supplementary equation (37)) depend on $g(\mathbf{r})$ in the uniform state, which we measure in experiments (Extended Data Fig. 9). Due to the higher probability of finding other particles in front of rather than behind the probe particle, the first contribution in equation (4a) gives a repulsion-induced force that opposes self-propulsion[5,11] (Fig. 4a). The higher the particle density, the higher the opposing force; the resulting density-induced slowdown produces standard self-trapping MIPS familiar from extensive theoretical study[1–6,9–11]. The second contribution in equation (4a) predicts a repulsion-induced force against density gradients, tending to homogenize particle concentration like a diffusive flux (Fig. 4a). Finally, the collective torque in equation (4b) tends to align particle orientation $\hat{\mathbf{n}}$ with the density gradient, thus reorienting

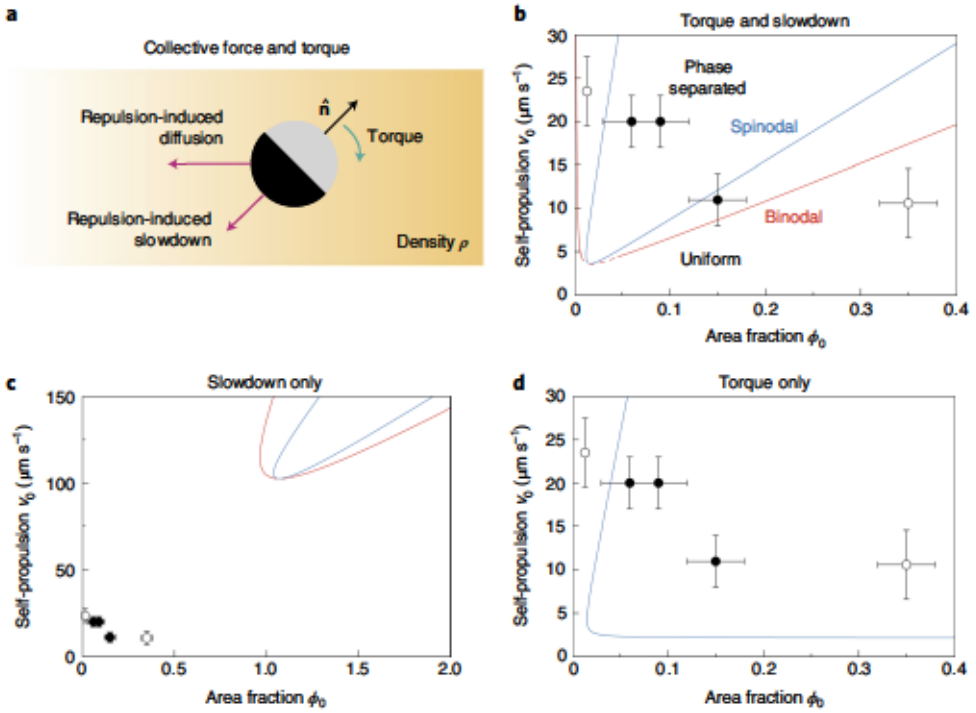

Fig. 4 | State diagram of torque-based active phase separation. a, In the theoretical model, a probe particle experiences collective interaction force and torque (equations (4a) and (4b)) in a particle density field $\rho(\mathbf{r})$, which increases from left to right in this depiction. Repulsion leads to two collective forces (purple): one opposite to self-propulsion (slowdown), and one opposite to the density gradient (diffusion). Collective torques (green) tend to align particle motion with density gradients. **b**, State boundaries (curves) predicted using experimental estimates for parameter values (Supplementary Table 1). The numerically unresolved region of the binodal near the critical point is indicated by a dashed curve as a guide to the eye. The filled and open data points show the experimental conditions for which phase separation was observed or not, respectively. **c**, State diagram predicted from slowdown only, that is $\tau_1 = 0$. Note the different scale from **b**. **d**, State diagram predicted from torques only, that is $\zeta_0 = 0$. Note the absence of a binodal in this case. Error bars are s.d. obtained as in Fig. 2c.

particle motion towards higher-density regions (Fig. 4a), as observed at the cluster edges in experiments (Fig. 1d–f). This collective torque requires non-reciprocity of the interparticle torques (equation (2)). Reciprocal torques, such as $\boldsymbol{\Gamma}_{ij} \propto \hat{\mathbf{n}}_i \times \hat{\mathbf{n}}_j$, could not orient particles towards the location of other particles, and hence $\boldsymbol{\Gamma}_{\mathrm{int}}$ would vanish[23,24] (Supplementary Note B). Finally, while non-reciprocal torques can lead to chiral phases[38], we do not find them here.

Torque-based phase separation

As particles reorient towards crowded areas, they self-propel up their own density gradient (Fig. 4a). Hence, particles migrate towards crowded regions, which produces an instability promoting phase separation. Similar behaviour was observed in active agents with finite vision cones[39–41]. To predict the instability, we complete the coarse-graining and obtain hydrodynamic equations (Supplementary Note B). The density field follows a continuity equation,

$$\partial_t \rho = -\boldsymbol{\nabla} \cdot \mathbf{J}; \qquad \mathbf{J} = v[\rho]\mathbf{p} - (D_{\mathrm{t}} + D_{\mathrm{rep}}[\rho])\boldsymbol{\nabla}\rho, \tag{5}$$

where the flux includes contributions from self-propulsion at a density-dependent speed $v[\rho(\mathbf{r})] = v_0 - \zeta_0\rho(\mathbf{r})/\xi_{\mathrm{t}}$, and diffusion that combines both bare and repulsion-induced diffusivities, D_{t} and $D_{\mathrm{rep}}[\rho(\mathbf{r})] = \zeta_1\rho(\mathbf{r})/\xi_{\mathrm{t}}$, respectively. At times $t \gg D_{\mathrm{r}}^{-1}$, the polarity field $\mathbf{p}$ becomes slaved to the density field (Supplementary Note C):

$$\mathbf{p} = \frac{1}{2D_{\mathrm{r}}}\left(v_{\mathrm{tor}}[\rho]\boldsymbol{\nabla}\rho - \boldsymbol{\nabla}(v[\rho]\rho)\right), \tag{6}$$

where the density-dependent speed $v_{\mathrm{tor}}[\rho(\mathbf{r})] = \tau_1\rho(\mathbf{r})/\xi_{\mathrm{r}}$ embodies the effects of torques in polarizing the system towards increasing densities. Introducing equation (6) into equation (5), we obtain $\mathbf{J} = -\mathcal{D}[\rho]\boldsymbol{\nabla}\rho$, where

$$\mathcal{D}[\rho] = D_{\mathrm{t}} + D_{\mathrm{rep}}[\rho] + \frac{v[\rho]}{2D_{\mathrm{r}}}\left(v[\rho] + v'[\rho]\rho - v_{\mathrm{tor}}[\rho]\right) \tag{7}$$

is a collective diffusivity. Thus, a uniform state with density ρ_0 experiences a spinodal instability for $\mathcal{D}(\rho_0) < 0$. In the absence of interaction torques ($v_{\mathrm{tor}}[\rho] = 0$), $\mathcal{D}$ can turn negative due to repulsion-induced slowdown ($v'[\rho] < 0$), which is the standard mechanism for MIPS[1]. Here, equation (7) shows that, even in the absence of slowdown ($v'[\rho] = 0$), torques alone ($v_{\mathrm{tor}}[\rho] > 0$) can produce a MIPS-like instability.

Furthermore, we establish that the torque-induced instability leads to phase coexistence. To this end, we express the particle flux $\mathbf{J}$ as deriving from an effective chemical potential $\mu[\rho]$ (refs. [1,42–48]): $\mathbf{J} = -M[\rho]\nabla\mu[\rho]$, with $M[\rho]$ the mobility functional (Supplementary Note C). We then use the relation $f'(\rho) = \mu(\rho)$ to obtain a local effective free energy $f(\rho)$, which has the conventional double-well shape (Extended Data Fig. 10). Ignoring non-local corrections[1,43,47,48], we use the common-tangent construction on $f(\rho)$ to predict the densities of the coexisting phases, that is the binodal lines of the phase diagram (Supplementary Note C). Importantly, our theory predicts that these uniform-density phases have no orientational order (see equation (6)). Our theory is approximate; hence, we do not expect the predicted binodal lines to be quantitatively accurate. Yet, the existence of phase coexistence is a robust prediction, which relies on only two ingredients: the torques towards dense regions and the decrease of particle speed at high densities (Supplementary Note C). In our experiments, clusters do not achieve uniform bulk density

(Fig. 1f), and therefore we are unable to observe the predicted phase coexistence. This fact suggests to us that the experimental system is in a dynamical regime whose asymptotic behaviour at very large cluster size has not yet been achieved.

To compare our predictions with experiments, we estimate the values of all the model parameters, including the particles' translational and rotational diffusion and friction coefficients, as well as the strength of the electric dipoles (Supplementary Note D). These estimates allow us to predict the phase diagram in the conditions of our experiments. Our experimental observations of phase separation fall within the predicted region of the phase diagram when we include both the slowdown and torque effects (Fig. 4b). Similarly, the absence of phase separation at high area fraction also agrees with our predictions (Fig. 4b). In the uniform high-density state, we observe transient particle chains throughout the system (Supplementary Video 6). With slowdown only, we cannot account for our experimental observations: the predicted phase-separation region lies at much higher self-propulsion speeds and densities than experimentally observed (Fig. 4c). Conversely, while torques alone can account for the instability of the uniform phase (spinodal in Fig. 4d), they do not yield phase coexistence (no binodal in Fig. 4d). Repulsion-induced slowdown is required to stabilize the dense phase.

We have demonstrated a new type of active phase separation based on non-reciprocal torques. Active agents reorient themselves towards crowded areas to form structured clusters, while moving easily within clusters and also into and out of them. Perhaps more fundamentally, our theory shows that orientational interactions (torques) can produce phases of matter without internal orientational order. Our work thus establishes connections between the paradigms of aligning and non-aligning active matter, contributing to the understanding of how different types of interparticle interaction can yield qualitatively new kinds of collective non-equilibrium phenomena[49–52].

Online content

Any methods, additional references, Nature Research reporting summaries, source data, extended data, supplementary information, acknowledgements, peer review information; details of author contributions and competing interests; and statements of data and code availability are available at https://doi.org/10.1038/s41567-021-01238-8.

Received: 9 November 2020; Accepted: 6 April 2021;
Published online: 20 May 2021

References

1. Cates, M. E. & Tailleur, J. Motility-induced phase separation. *Annu. Rev. Condens. Matter Phys.* **6**, 219–244 (2015).
2. Gonnella, G., Marenduzzo, D., Suma, A. & Tiribocchi, A. Motility-induced phase separation and coarsening in active matter. *C. R. Phys.* **16**, 316–331 (2015).
3. Marchetti, M. C., Fily, Y., Henkes, S., Patch, A. & Yllanes, D. Minimal model of active colloids highlights the role of mechanical interactions in controlling the emergent behavior of active matter. *Curr. Opin. Colloid Interface Sci.* **21**, 34–43 (2016).
4. Zöttl, A. & Stark, H. Emergent behavior in active colloids. *J. Phys. Condens. Matter* **28**, 253001 (2016).
5. Speck, T. Collective forces in scalar active matter. *Soft Matter* **16**, 2652–2663 (2020).
6. Ma, Z., Yang, M. & Ni, R. Dynamic assembly of active colloids: theory and simulation. *Adv. Theory Simul.* **3**, 2000021 (2020).
7. Tailleur, J. & Cates, M. E. Statistical mechanics of interacting run-and-tumble bacteria. *Phys. Rev. Lett.* **100**, 218103 (2008).
8. Rein, M., Heinß, N., Schmid, F. & Speck, T. Collective behavior of quorum-sensing run-and-tumble particles under confinement. *Phys. Rev. Lett.* **116**, 058102 (2016).
9. Fily, Y. & Marchetti, M. C. Athermal phase separation of self-propelled particles with no alignment. *Phys. Rev. Lett.* **108**, 235702 (2012).
10. Redner, G. S., Hagan, M. F. & Baskaran, A. Structure and dynamics of a phase-separating active colloidal fluid. *Phys. Rev. Lett.* **110**, 055701 (2013).
11. Bialké, J., Löwen, H. & Speck, T. Microscopic theory for the phase separation of self-propelled repulsive disks. *Europhys. Lett.* **103**, 30008 (2013).
12. Aranson, I. S. Active colloids. *Phys. Usp.* **56**, 79–92 (2013).
13. Bechinger, C. et al. Active particles in complex and crowded environments. *Rev. Mod. Phys.* **88**, 045006 (2016).
14. Zhang, J., Luijten, E., Grzybowski, B. A. & Granick, S. Active colloids with collective mobility status and research opportunities. *Chem. Soc. Rev.* **46**, 5551–5569 (2017).
15. Theurkauff, I., Cottin-Bizonne, C., Palacci, J., Ybert, C. & Bocquet, L. Dynamic clustering in active colloidal suspensions with chemical signaling. *Phys. Rev. Lett.* **108**, 268303 (2012).
16. Palacci, J., Sacanna, S., Steinberg, A. P., Pine, D. J. & Chaikin, P. M. Living crystals of light-activated colloidal surfers. *Science* **339**, 936–940 (2013).
17. Buttinoni, I. et al. Dynamical clustering and phase separation in suspensions of self-propelled colloidal particles. *Phys. Rev. Lett.* **110**, 238301 (2013).
18. Ginot, F., Theurkauff, I., Detcheverry, F., Ybert, C. & Cottin-Bizonne, C. Aggregation–fragmentation and individual dynamics of active clusters. *Nat. Commun.* **9**, 696 (2018).
19. Geyer, D., Martin, D., Tailleur, J. & Bartolo, D. Freezing a flock: motility-induced phase separation in polar active liquids. *Phys. Rev. X* **9**, 031043 (2019).
20. van der Linden, M. N., Alexander, L. C., Aarts, D. G. A. L. & Dauchot, O. Interrupted motility induced phase separation in aligning active colloids. *Phys. Rev. Lett.* **123**, 098001 (2019).
21. Shi, X.-q. & Chaté, H. Self-propelled rods: linking alignment-dominated and repulsion-dominated active matter. Preprint at https://arxiv.org/abs/1807.00294 (2018).
22. van Damme, R., Rodenburg, J., van Roij, R. & Dijkstra, M. Interparticle torques suppress motility-induced phase separation for rodlike particles. *J. Chem. Phys.* **150**, 164501 (2019).
23. Jayaram, A., Fischer, A. & Speck, T. From scalar to polar active matter: connecting simulations with mean-field theory. *Phys. Rev. E* **101**, 022602 (2020).
24. Großmann, R., Aranson, I. S. & Peruani, F. A particle–field approach bridges phase separation and collective motion in active matter. *Nat. Commun.* **11**, 5365 (2020).
25. Bär, M., Großmann, R., Heidenreich, S. & Peruani, F. Self-propelled rods: insights and perspectives for active matter. *Annu. Rev. Condens. Matter Phys.* **11**, 441–466 (2020).
26. Pu, M., Jiang, H. & Hou, Z. Reentrant phase separation behavior of active particles with anisotropic Janus interaction. *Soft Matter* **13**, 4112–4121 (2017).
27. Liao, G.-J., Hall, C. K. & Klapp, S. H. L. Dynamical self-assembly of dipolar active Brownian particles in two dimensions. *Soft Matter* **16**, 2208–2223 (2020).
28. Farrell, F. D. C., Marchetti, M. C., Marenduzzo, D. & Tailleur, J. Pattern formation in self-propelled particles with density-dependent motility. *Phys. Rev. Lett.* **108**, 248101 (2012).
29. Barré, J., Chétrite, R., Muratori, M. & Peruani, F. Motility-induced phase separation of active particles in the presence of velocity alignment. *J. Stat. Phys.* **158**, 589–600 (2014).
30. Sesé-Sansa, E., Pagonabarraga, I. & Levis, D. Velocity alignment promotes motility-induced phase separation. *Europhys. Lett.* **124**, 30004 (2018).
31. Bhattacherjee, B. & Chaudhuri, D. Re-entrant phase separation in nematically aligning active polar particles. *Soft Matter* **15**, 8483–8495 (2019).
32. Gangwal, S., Cayre, O. J., Bazant, M. Z. & Velev, O. D. Induced-charge electrophoresis of metallodielectric particles. *Phys. Rev. Lett.* **100**, 058302 (2008).
33. Moran, J. L. & Posner, J. D. Phoretic self-propulsion. *Annu. Rev. Fluid Mech.* **49**, 511–540 (2017).
34. Yan, J. et al. Reconfiguring active particles by electrostatic imbalance. *Nat. Mater.* **15**, 1095–1099 (2016).
35. Poncet, A., Bénichou, O., Démery, V. & Nishiguchi, D. Pair correlation of dilute active Brownian particles: from low-activity dipolar correction to high-activity algebraic depletion wings. *Phys. Rev. E* **103**, 012605 (2021).
36. Kirkwood, J. G., Buff, F. P. & Green, M. S. The statistical mechanical theory of transport processes. III. The coefficients of shear and bulk viscosity of liquids. *J. Chem. Phys.* **17**, 988–994 (1949).
37. Irving, J. H. & Kirkwood, J. G. The statistical mechanical theory of transport processes. IV. The equations of hydrodynamics. *J. Chem. Phys.* **18**, 817–829 (1950).
38. Fruchart, M., Hanai, R., Littlewood, P. B. & Vitelli, V. Non-reciprocal phase transitions. *Nature* **592**, 363–369 (2021).
39. Barberis, L. & Peruani, F. Large-scale patterns in a minimal cognitive flocking model: incidental leaders, nematic patterns, and aggregates. *Phys. Rev. Lett.* **117**, 248001 (2016).

40. Durve, M., Saha, A. & Sayeed, A. Active particle condensation by non-reciprocal and time-delayed interactions. *Eur. Phys. J. E* **41**, 49 (2018).
41. Lavergne, F. A., Wendehenne, H., Bäuerle, T. & Bechinger, C. Group formation and cohesion of active particles with visual perception-dependent motility. *Science* **364**, 70–74 (2019).
42. Stenhammar, J., Tiribocchi, A., Allen, R. J., Marenduzzo, D. & Cates, M. E. Continuum theory of phase separation kinetics for active Brownian particles. *Phys. Rev. Lett.* **111**, 145702 (2013).
43. Wittkowski, R. et al. Scalar ϕ^4 field theory for active-particle phase separation. *Nat. Commun.* **5**, 4351 (2014).
44. Speck, T., Bialké, J., Menzel, A. M. & Löwen, H. Effective Cahn–Hilliard equation for the phase separation of active Brownian particles. *Phys. Rev. Lett.* **112**, 218304 (2014).
45. Speck, T., Menzel, A. M., Bialké, J. & Löwen, H. Dynamical mean-field theory and weakly non-linear analysis for the phase separation of active Brownian particles. *J. Chem. Phys.* **142**, 224109 (2015).
46. Paliwal, S., Rodenburg, J., van Roij, R. & Dijkstra, M. Chemical potential in active systems: predicting phase equilibrium from bulk equations of state? *New J. Phys.* **20**, 015003 (2018).
47. Solon, A. P., Stenhammar, J., Cates, M. E., Kafri, Y. & Tailleur, J. Generalized thermodynamics of phase equilibria in scalar active matter. *Phys. Rev. E* **97**, 020602 (2018).
48. Solon, A. P., Stenhammar, J., Cates, M. E., Kafri, Y. & Tailleur, J. Generalized thermodynamics of motility-induced phase separation: phase equilibria, Laplace pressure, and change of ensembles. *New J. Phys.* **20**, 075001 (2018).
49. Marchetti, M. C. et al. Hydrodynamics of soft active matter. *Rev. Mod. Phys.* **85**, 1143–1189 (2013).
50. Hagan, M. F. & Baskaran, A. Emergent self-organization in active materials. *Curr. Opin. Cell Biol.* **38**, 74–80 (2016).
51. Fodor, É. & Marchetti, M. C. The statistical physics of active matter: from self-catalytic colloids to living cells. *Physica A* **504**, 106–120 (2018).
52. Shaebani, M. R., Wysocki, A., Winkler, R. G., Gompper, G. & Rieger, H. Computational models for active matter. *Nat. Rev. Phys.* **2**, 181–199 (2020).

Methods

Particle synthesis. Following protocols described elsewhere[34], a submonolayer of 3-μm-diameter silica particles (Tokuyama) is prepared on a standard glass slide. To obtain metal–dielectric Janus particles, 20 nm of titanium and then 5 nm of SiO_2 are deposited vertically on the glass slide using an electron-beam evaporator. The preparation is washed with isopropyl alcohol and deionized water, and then sonicated into deionized water to collect the Janus particles.

Experimental set-up. NaCl stock solution is added to the particle suspension to obtain 0.05 mM NaCl solutions. The particle suspensions are confined between two coverslips (SPI Supplies) coated with indium tin oxide to make them conductive, and with 25 nm of silicon oxide to prevent particles from sticking to them. The coverslips have a 9 mm hole in the centre, separated by a 120-μm-thick spacer (Grace Bio-Labs SecureSeal). An alternating voltage is applied between the coverslips using a function generator (Agilent 33522A). The sample cell is imaged with ×5 and ×40 air objectives on an inverted microscope (Axiovert 200). Microscopic images and videos are taken with a CMOS (complementary metal–oxide–semiconductor) camera (Edmund Optics 5012M GigE) with 20 ms time resolution.

Image analysis. Image processing is performed using MATLAB with home-developed codes.

Data availability

Source data are provided with this paper. All other data that support the plots and findings of this study are available from the authors upon request.

Code availability

All codes are available from the authors upon request.

Acknowledgements

J.Z. and S.G. were supported by the taxpayers of South Korea through the Institute of Basic Science, project code IBS-R020-D1. R.A. thanks J. Tailleur for insightful discussions, and acknowledges discussions with the participants of the virtual 'Active 20' KITP programme, supported in part by the National Science Foundation under grant no. NSF PHY-1748958. R.A. acknowledges support from the Human Frontier Science Program (LT000475/2018-C). J.Y. holds a Career Award at the Scientific Interface from the Burroughs Wellcome Fund. N.S.W. acknowledges support from the National Science Foundation, through the Center for the Physics of Biological Function (PHY-1734030).

Author contributions

J.Z., J.Y. and S.G. conceived the experiment. J.Z. performed the experiments and analysed data with help from J.Y. R.A. conceived and developed the theory and analysed data. N.S.W. supervised the theory. All authors discussed and interpreted the results. J.Z., R.A., N.S.W. and S.G. wrote the manuscript.

Competing interests

The authors declare no competing interests.

Additional information

Extended data is available for this paper at https://doi.org/10.1038/s41567-021-01238-8.

Supplementary information The online version contains supplementary material available at https://doi.org/10.1038/s41567-021-01238-8.

Correspondence and requests for materials should be addressed to S.G.

Peer review information *Nature Physics* thanks the anonymous reviewers for their contribution to the peer review of this work.

Reprints and permissions information is available at www.nature.com/reprints.

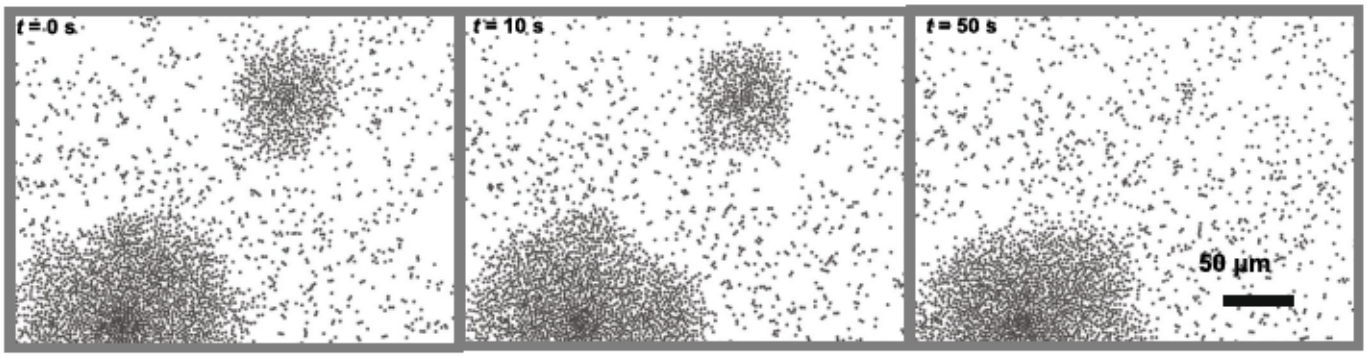

Extended Data Fig. 1 | Ostwald ripening of active colloids. Series of snapshots showing a small cluster shrinking and disappearing as part of the coarsening process.

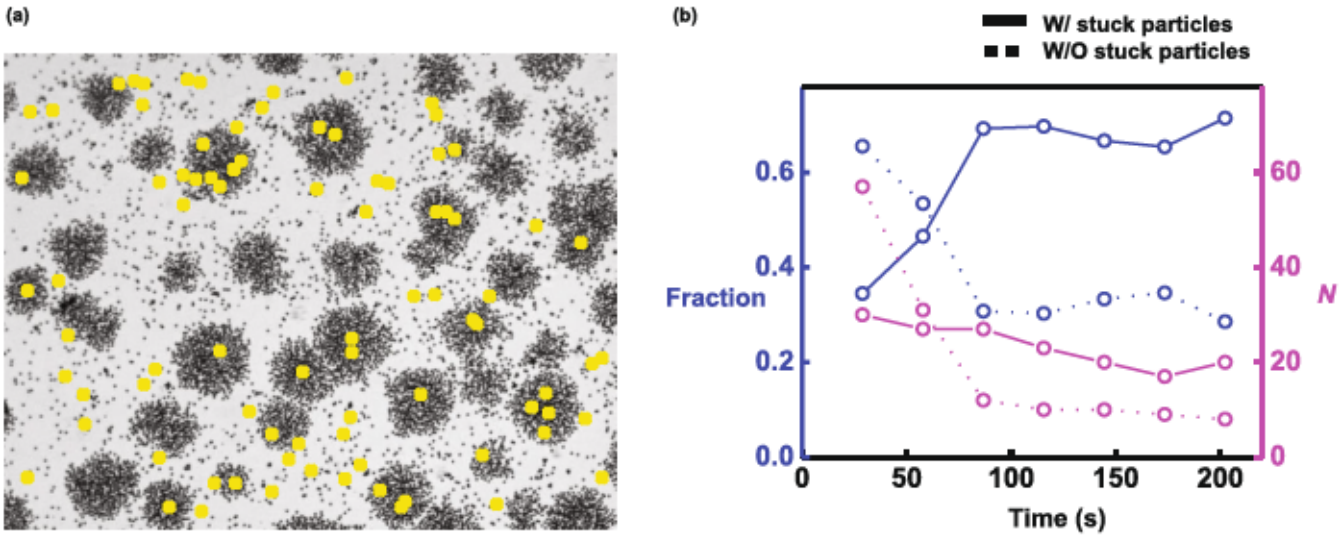

Extended Data Fig. 2 | Clusters with and without stuck particles. a, A bright field microscopy image of active phase separation in a late stage with yellow stars labelling particles that, stuck to the coverslip, remain in the same location throughout the experiment. **b**, The number (magenta) and fraction (blue) of clusters with and without (solid and dotted curves, respectively) at least one stuck particle. In the beginning of the experiment, more clusters are formed without than with stuck particles. With elapsed time, the number of clusters forming both with and without stuck particles decreases (magenta), but clusters with stuck particles become the most abundant.

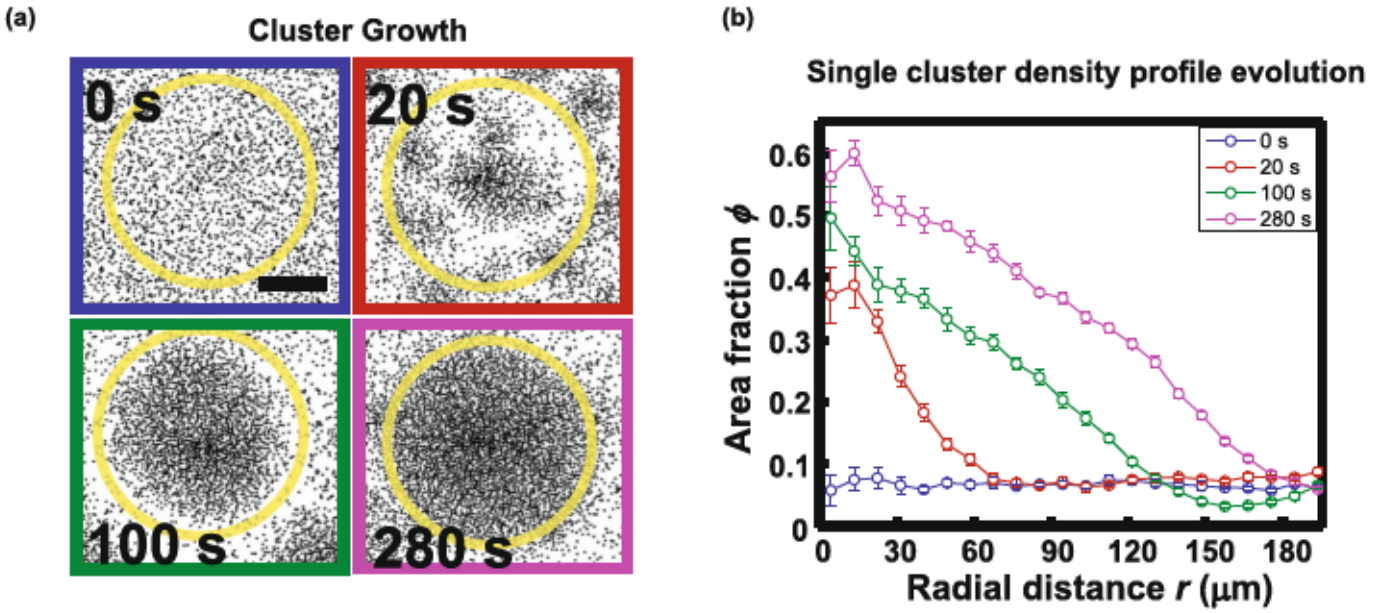

Extended Data Fig. 3 | Dynamics of cluster growth. a, Snapshots of cluster growth upon a.c. electric field application (Supplementary Movie 2). Scale bar, 100 μm. The yellow circumference indicates the outline of the cluster in the final snapshot. **b**, Density profile evolution in the growing cluster shown in a. Averages are over 20 frames (1.2 s) centered at each designated time point. Error bars are s.d.

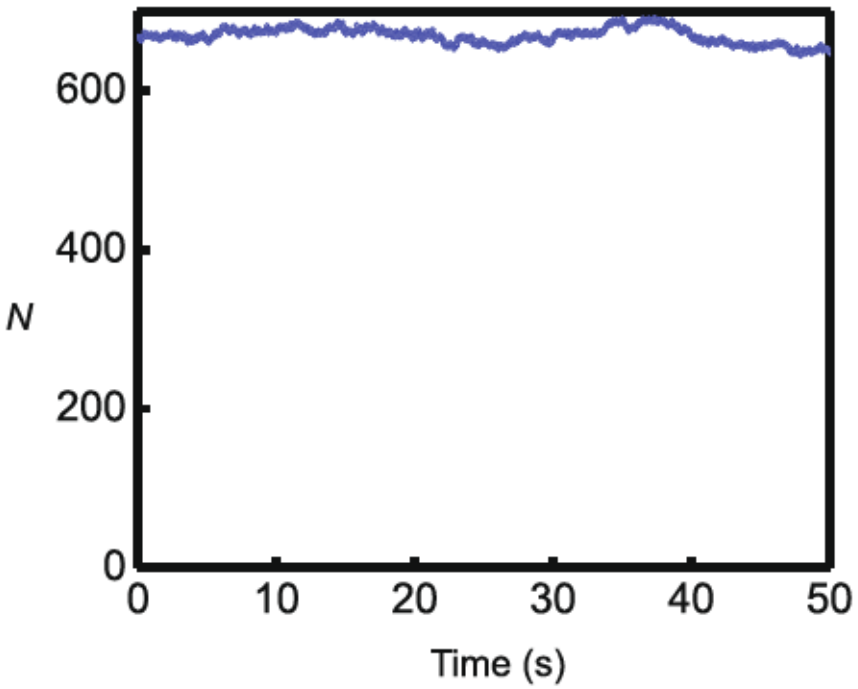

Extended Data Fig. 4 | Particle-number fluctuations in a quasi-steady state cluster. The number of particles in this cluster, the same cluster also shown in Figs. 1 and 2, remains roughly constant during the time when averages are taken.

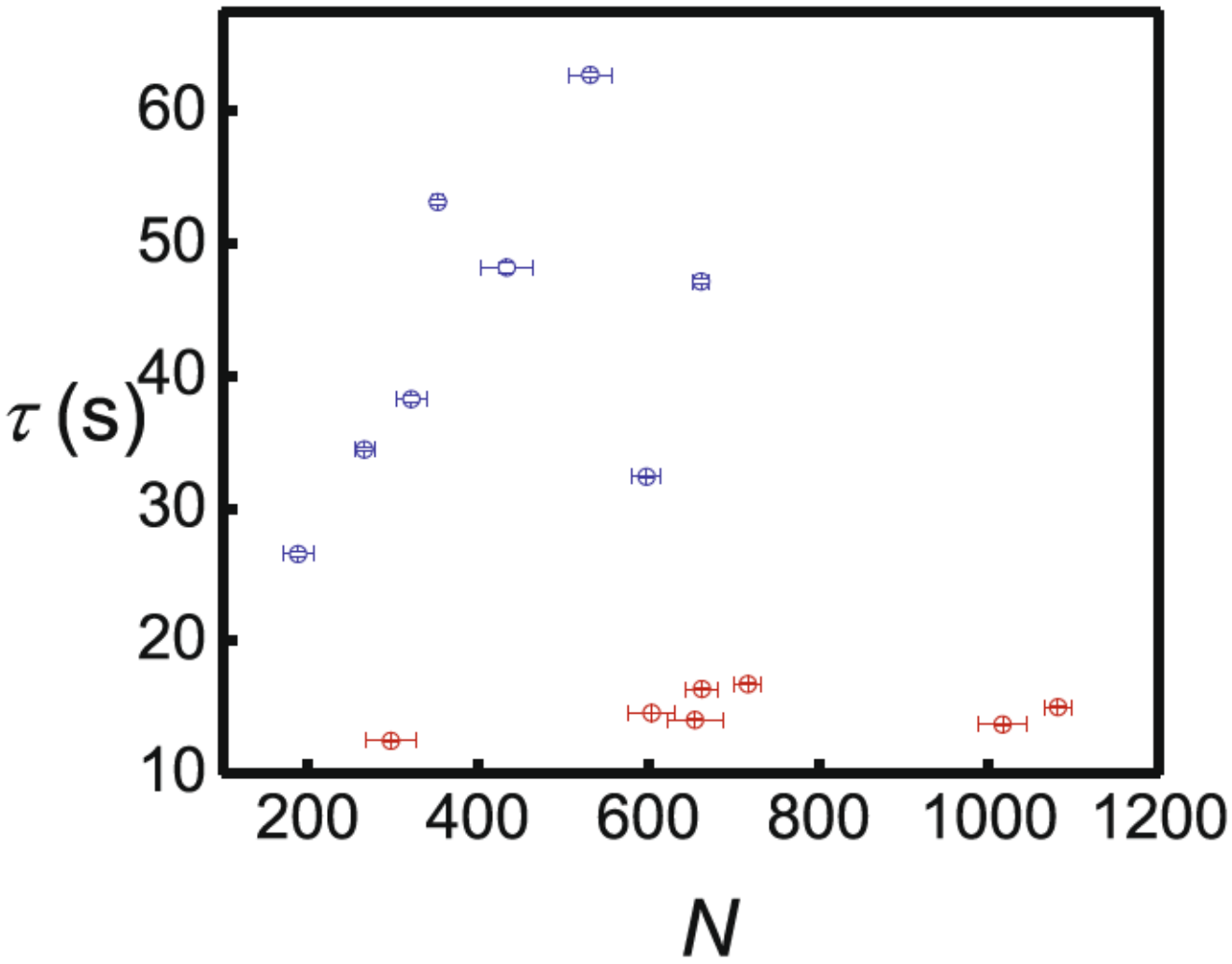

Extended Data Fig. 5 | Particle turnover time depends on cluster size and particle speed. The turnover time τ, defined in Fig. 2b, depends on the number of particles N in the cluster, and on particle speed and interactions. The number of particles is averaged over the time used to calculate the turnover time τ as in Fig. 2b. This averaging time varies from 30 to 180 s in different clusters. Error bars are s.d. Blue points correspond to an applied electric field with amplitude 66 V/mm and frequency 30 kHz, producing an average single-particle speed of 12 μm/s within clusters. Red points correspond to a field with the same frequency but amplitude 83 V/mm, giving an average single-particle speed of 22 μm/s within clusters. Particles with higher speeds and stronger interactions turn over more quickly.

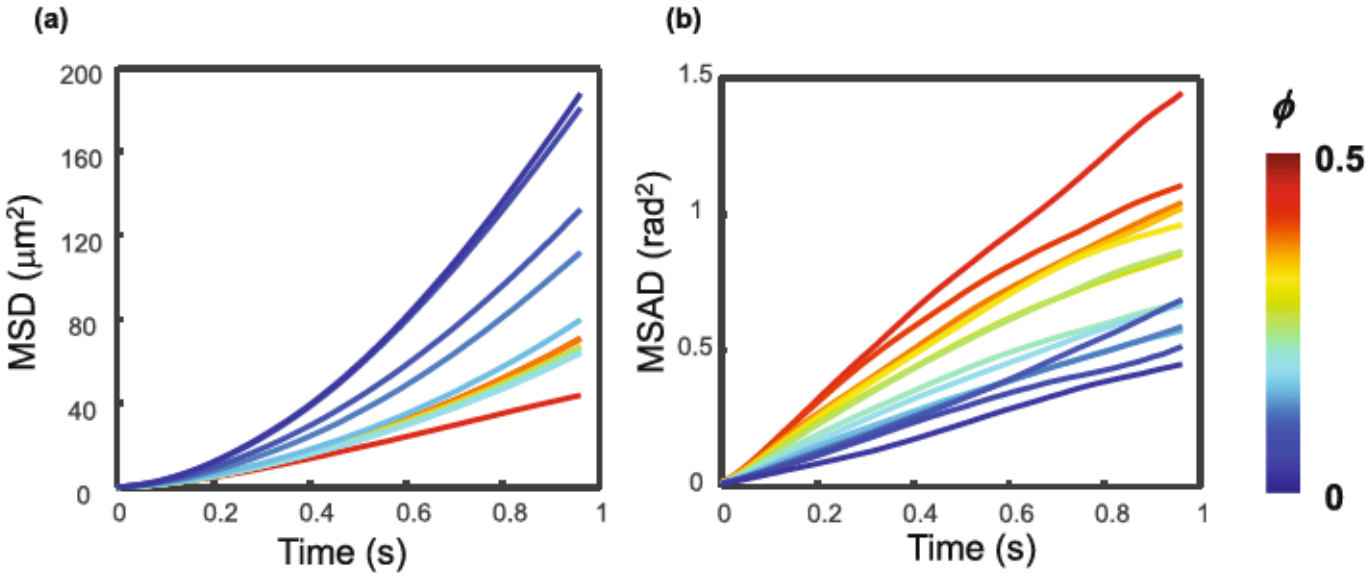

Extended Data Fig. 6 | Mean square displacements. Mean square displacements of particle position (**a**) and angle (**b**) for particles at different local area fractions ϕ. The particle speed and effective rotational diffusivity shown in Fig. 2c are obtained from the first 0.5 s of these data by fitting $\mathrm{MSD} = (vt)^2$ and $\mathrm{MSAD} = D_r^{\mathrm{eff}} t$, respectively.

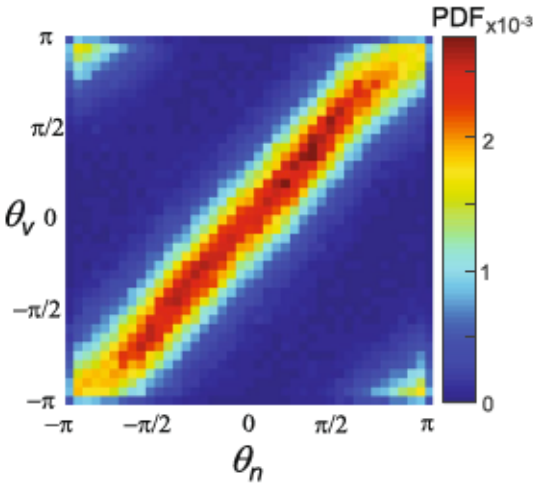

Extended Data Fig. 7 | Orientation-velocity coincidence prior to clustering. Joint probability distribution function (PDF) of the particle orientation and velocity angles, as defined in Fig. 3d, prior to cluster formation. In contrast to the mismatch found in clusters (Figs. 3e and 3f), the orientation and velocity directions coincide before clusters form.

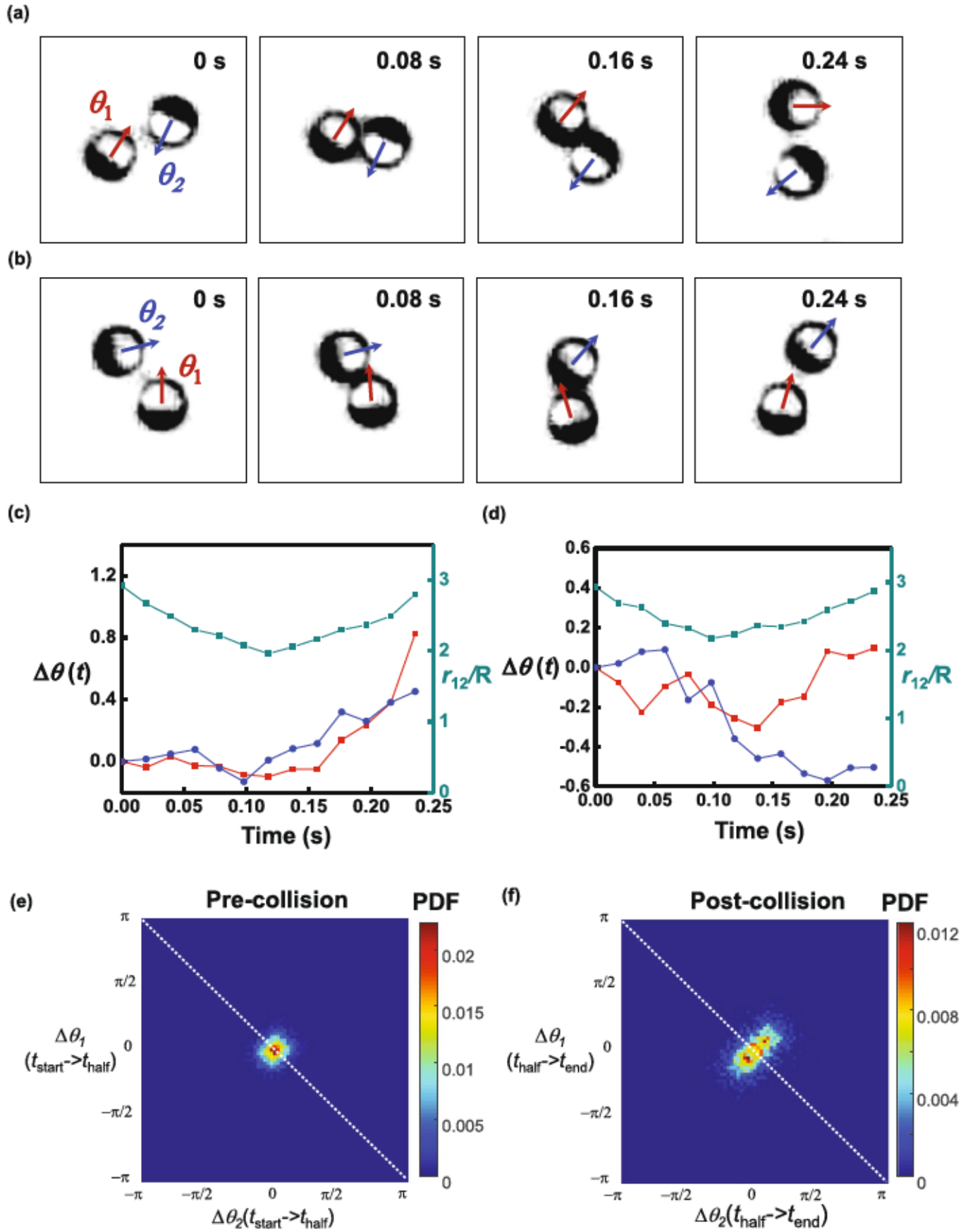

Extended Data Fig. 8 | See next page for caption.

Extended Data Fig. 8 | Dynamics and statistics of two-particle interaction events. a,**b**, Two examples of interaction events between two particles, which we define by the condition $r_{12} < 3R$, with R the particle radius. We also require the minimal interparticle distance to be min $r_{12} < 2.2R$. We analyzed 2061 of such interaction events. In **a**, both particles turn clockwise. Therefore, the interaction torque has the same sign on both particles, showing that torques are non-reciprocal ($\Gamma_{12} \neq -\Gamma_{21}$). This type of interaction with particles initially pointing in opposite directions, defined by the condition $|\theta_1(t=0)+\theta_2(t=0)| < 0.2$ rad, occurred in ~33% of the analyzed events. In **b**, particle 1 changes its orientation very little compared to particle 2, showing another example of non-reciprocal torques. The particles end up aligned in a chain. This type of interaction, defined by the condition $\min(\theta_1(t) - \theta_2(t)) < 0.5$ rad during the interaction event, occurred in ~2.8% of the analyzed events. **c**,**d**, Evolution of the interparticle distance, r_{12}, and the change in angle of each particle, $\Delta\theta_{1,2}$, for the interaction events in **a** and **b**, respectively. **e**,**f**, Joint probability distribution functions of the angle changes of each particle in an interacting pair. The pre-collision (**e**) and post-collision (**f**) phases respectively correspond to the times before and after the particles reach their minimal distance. These histograms show that, statistically, both particles in the interacting pair tend to turn in the same direction, showing that interaction torques are non-reciprocal. Reciprocal torques would lead to particles rotating in opposite directions and by the same magnitude, as indicated by the dashed lines.

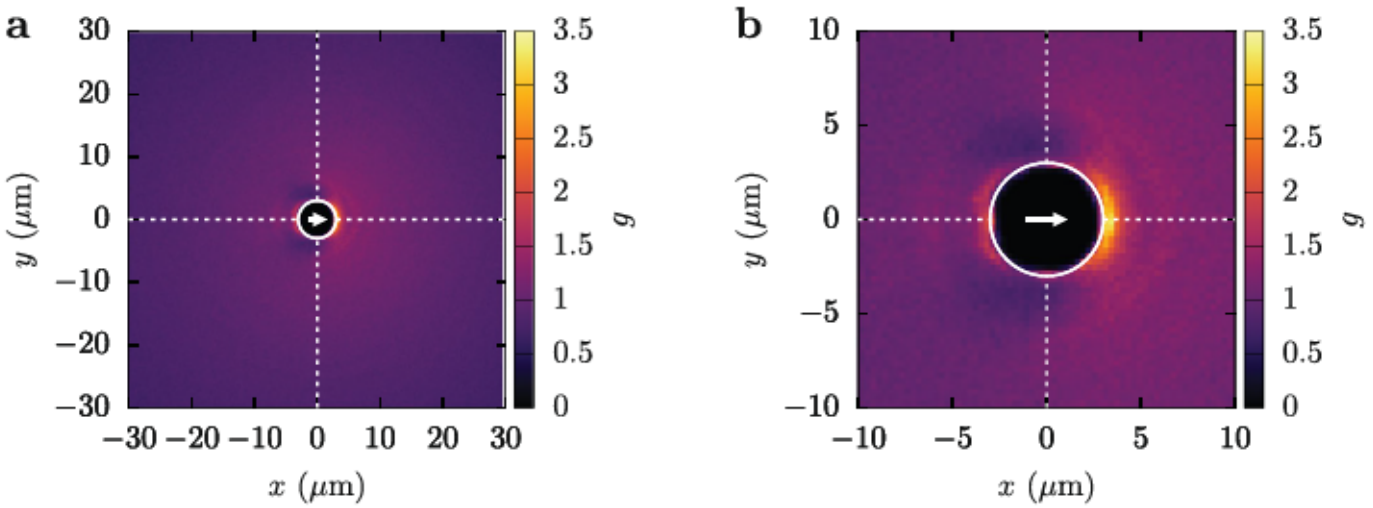

Extended Data Fig. 9 | Pair distribution function measured in experiments. a, Full $g(x, y)$ used in the calculation of the collective force and torque coefficients ζ_0, $\zeta_\parallel$ and τ_1 (see text and Supplementary Eq. (37)). **b**, Zoomed-in region, which allows to more clearly appreciate that the pair distribution function is anisotropic, indicating that it is more likely to find another particle in front than behind a reference self-propelled particle. In each panel, the arrow indicates the direction of self-propulsion of the reference particle, dashed lines indicate the coordinate axes, and the white circle indicates the region $r < 2R$ of volume exclusion between two particles.

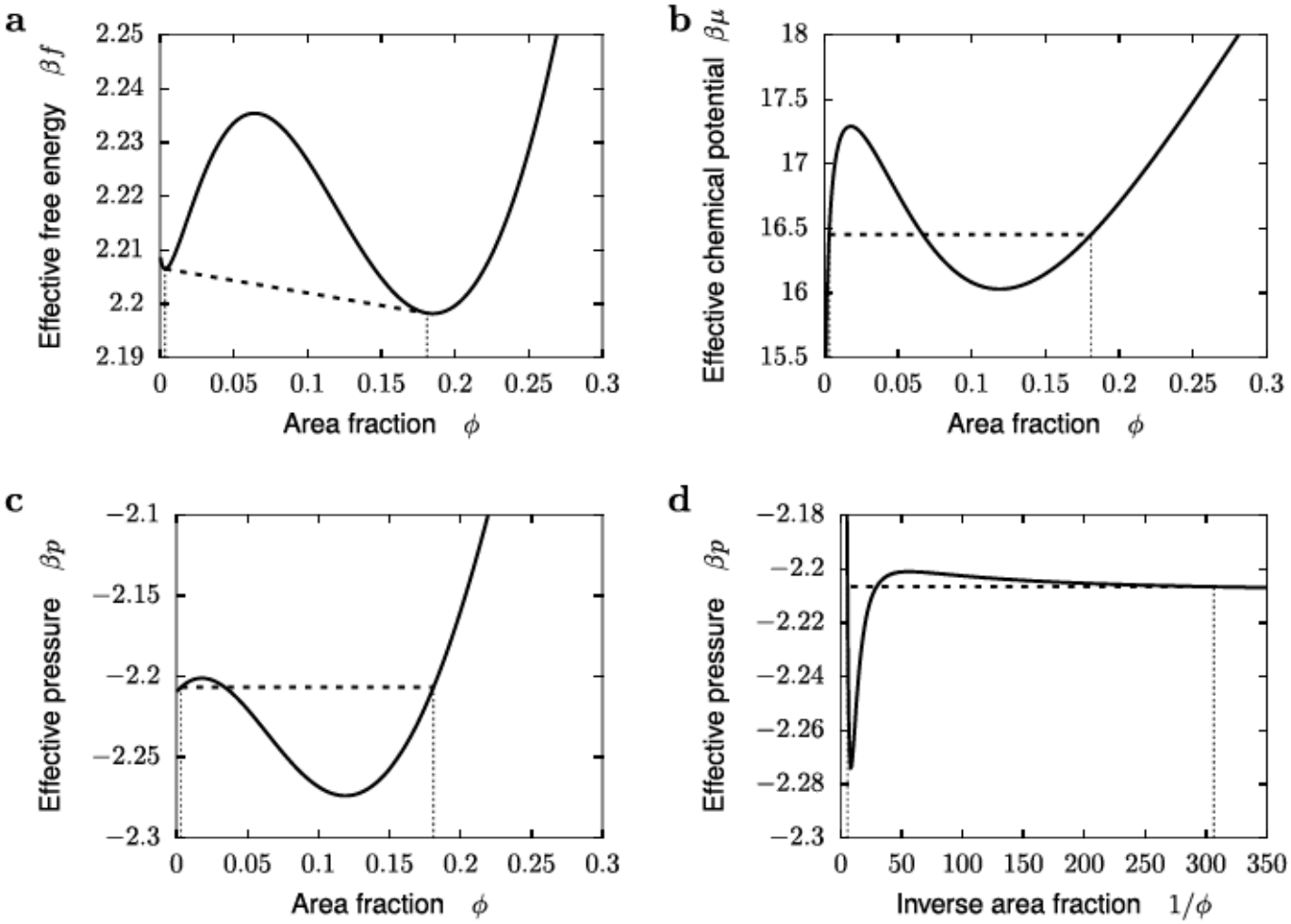

Extended Data Fig. 10 | Effective thermodynamics of torque-based MIPS. Effective free energy density (**a**, Supplementary Eq. (56)), chemical potential (**b**, Supplementary Eq. (55)), and thermodynamic pressure (**c**–**d**, Supplementary Eq. (57)) of the active Janus suspension as a function of the area fraction of particles, for $v_0 = 10$ μm/s. The remaining parameter values are evaluated using the estimates in Table I in the Supplementary Note. To better visualize the double-well shape of the free energy $\beta f(\phi)$, we added a linear term -16.5ϕ, which does not affect phase coexistence. Thin dashed lines indicate the densities of the coexisting phases. These densities are obtained from the common-tangent construction on the free energy density (**a**), which corresponds to equality of both chemical potential (**b**) and pressure (**c**), as indicated by thick dashed lines. Alternatively, the common-tangent construction also corresponds to the Maxwell construction on the curve $p(1/\phi)$, as indicated by the thick dashed line in panel **d**.